Dilute iron-doped polycrystalline strontium titanate: tracking iron valence and local interactions

Michael Knight[1], Ivar Reimanis[1,*], Abigail Meyer[2], Jan-Helmut Preusker[3], and
Wolfgang Rheinheimer[4]

[1]Metallurgical and Materials Engineering Department, Colorado School of Mines,
Golden, Colorado, United States of America

[2]Chemical and Biological Engineering Department, Colorado School of Mines,
Golden, Colorado,
United States of America

[3]Institute for Applied Materials: Ceramic Materials and Technologies, Karlsruhe
Institute of Technology, Karlsruhe, Germany

[4]Institute of Energy and Climate Research: Materials Synthesis and Processing,
Forschungszentrum
Jüelich, Jüelich, Germany

[*]Corresponding author: Ivar Reimanis, reimanis@mines.edu

Abstract

The mixed-valence states of dilute Fe (0.2mol%, 0.5mol%, and 1.2mol%) in bulk polycrystalline ($SrTiO_3$) (STO) were determined. Specimens were sintered in air or O_2 at 1500°C or 1300°C with the intent to quantify the rela- tive valence states of Fe in the context of understanding microstructure development of Fe-doped STO. Mössbauer spectroscopy, electron paramagnetic resonance spectroscopy, and magnetometry were combined to track changes in Fe valence, and Raman spectroscopy and X-ray diffraction were used to describe the associated structural changes. Small concentrations of $(\mathrm{Fe}_{\mathrm{Ti}}' - \mathrm{V}_{\mathrm{O}}^{\bullet\bullet})^{\bullet}$ defect associates were detected, but the majority of $\mathrm{Fe}_{\mathrm{Ti}}'$ acceptors are isolated from oxygen vacancies. As doping increases, negative exchange interactions increase, consistent with an increase in the concentration of $\mathrm{Fe}_{\mathrm{Ti}}' - \mathrm{O}_{\mathrm{O}}^{\times} - \mathrm{Fe}_{\mathrm{Ti}}'$ configurations. Additionally, the fraction of dopants existing as isovalent $\mathrm{Fe}_{\mathrm{Ti}}^{\times}$

increased with P_{O_2} of the sintering atmosphere and with total Fe content.

1 Introduction

Strontium titanate ($SrTiO_3$) (STO) has undergone extensive investigation for applications such as solid-state ionic conduction, memristors, thermoelectricity, superconductivity, and photocatalytic water splitting.(1, 2, 3, 4, 5) Lightly Fe-doped STO is commonly used as a model representative for acceptor-doped large band gap electroceramics. It is generally accepted that low concentrations of Fe-dopants in STO substitute for Ti^{4+} and can exist in 4+, 3+, or 2+ oxidation states depending on P_{O_2} and temperature.(6, 7, 8) When treated or prepared in oxidizing conditions, Fe^{3+} and Fe^{4+} are expected to be preferred if substituted for Ti^{4+}. The valence state of Fe is known to play a role in both the properties mentioned above. For sintering and grain growth of stontium titanate, the valence state of Fe is of importance as well, but only indirectly. For both processes, segregation and space charge are of central importance.(9, 10, 11, 12) Segregation and space charge are known to depend on the doping and oxidation state. (13)

The $\mathrm{SrTi}_{1-x}\mathrm{Fe}_x\mathrm{O}_{3-\delta}$ (STFO) system forms a solid-solution for all values of x and is a mixed ionic and electronic conductor (MIEC), especially for Fe-rich compositions ($x > 0.1$).(14) Zhou and Goodenough reported on the mixed valence character of Fe, which showed a general trend of the $\mathrm{Fe}^{3+}/\mathrm{Fe}^{4+}$ ratio increasing as Fe content increases from 10mol% to 95mol%.(15) Furthermore, they concluded that the transport and magnetic properties in this system are strongly

influenced by interactions between Fe cations. Such interactions in the lattice indicate that extending the properties of the STFO system to the dilute Fe-doped STO model system is inappropriate. It has been suggested that only Fe doping concentrations less than 1-2mol% can be considered dilute, because at higher concentrations, there are significant Fe electronic states that overlap with one another and admix with O 2p valence states.(14, 15, 16)

Charge compensation for $\mathrm{Fe}_{\mathrm{Ti}}'$ acceptors occurs in the lattice by formation of $\mathrm{V}_{\mathrm{O}}^{\bullet\bullet}$.(17) Electroneutrality requires that

the compensating $\mathrm{V}_{\mathrm{O}}^{\bullet\bullet}$ concentration be half the Fe^{3+} concentration.(6) Therefore, even if strong electrostatic attraction of the oppositely charged defects exists, only half of the dilute $\mathrm{Fe}_{\mathrm{Ti}}'$ defects can have a $\mathrm{V}_{\mathrm{O}}^{\bullet\bullet}$ in the first coordination shell.

For Fe concentrations <0.3mol%, electron paramagnetic resonance (EPR) measurements show that the tendency for a $\mathrm{V}_{\mathrm{O}}^{\bullet\bullet}$ to be located in the first coordination shell of $\mathrm{Fe}_{\mathrm{Ti}}'$ decreases with increasing Fe content.(18) EPR results of Drahus *et at.* suggest that, when prepared in air, and when the Fe doping concentration is below 1mol%, the majority of Fe cations are present as Fe^{3+}(19), though the valence state would be expected to depend on the P_{O_2} and temperature.

Additionally, the same authors also verified the presence of a small concentration of the $\mathrm{Fe}_{\mathrm{Ti}}' - \mathrm{V}_{\mathrm{O}}^{\bullet\bullet}\ ^{\bullet}$ defect complex.

The valency changes of Fe have been observed experimentally, mostly by observing the optical changes associated with the $\mathrm{Fe}^{3+}/\mathrm{Fe}^{4+}$ transition,(20, 21, 22) but also by conductivity changes(23, 24). Generally, Fe^{4+} occurs in oxidized strontium titanate at low temperature. Defect structures have been observed widely in the presence of electric fields because of their technological relevance for dielectrics and their degradation(25, 26) and for memory applications (resistive switching(27)). The application of an electric field causes an oxygen vacancy migration towards the cathode (11, 23, 28), resulting in various changes of the defect structure (7, 29). For Fe-doped strontium titanate, this process involves a change of the valency of Fe, resulting in a color change (electrocoloration)(22, 28, 29). The valence change is well-documented by spectroscopic methods.(29)

It is well established that concentrations of acceptor defects increase in STO GB regions.(31, 32, 33) However, the use of spatially resolved spectroscopic techniques to directly observe segregation is difficult when the acceptor concentration is very low. The present work combines Mössbauer spectroscopy, EPR spectroscopy, and magnetometry to characterize Fe valence states in bulk polycrystalline STO with 0.2mol%, 0.5mol%, and 1.2mol% substituted for Ti. Long-range magnetic ordering of Fe in the bulk lattice is avoided by doping at such low concentrations and paramagnetic behavior of the dopants is expected. Mössbauer spectroscopy is useful for identifying the number of unique Fe sites in the system. Magnetometry is useful for estimating overall effective valence of paramagnetic species, as well as detecting exchange interactions between them. In particular, superconducting quantum interference device (SQUID) magnetometers are highly sensitive and capable of detecting very low concentrations of magnetic moments. Additionally, EPR spectroscopy is highly sensitive and can identify specific valence states, but under common X-band microwave excitation, only Kramers ions are detectable, *e.g.*, Fe^{3+} but not $Fe^{2+/4+}$.(19, 34) Combining all three experimental techniques is demonstrated here to provide a comprehensive method for estimating mixed-valence character and detecting local interactions of dilute Fe in polycrystalline STO.

The techniques are applied in the present work with the goal to describe defect states during the sintering and microstructure development of STO. It has been previously observed that grain growth in STO displays an anomalous behavior in which the grain growth rate decreases at temperatures above about 1400°C.(35) In the present experiments, two sintering temperatures, 1300°C and 1500°C were chosen in order to establish whether or not the defect states vary for STO sintered in the normal versus anomalous regimes. Initially, the samples were planned to only be sintered in air atmosphere, however, it was discovered that sintering in O_2 atmosphere improves densification. This is due to the high oxygen diffusion in strontium titanate, which eases pore shrinkage during final stage sintering compared to sintering in air, i.e. with a high nitrogen content. The authors acknowledge the small absolute difference in P_{O_2} between the two atmospheres, however, this small difference provided an opportunity to probe the precision of the magnetic characterization techniques employed here.

2 Experimental

$Sr(Ti_{1-x}Fe_x)O_{3-\delta}$ powders with x = 0.002*,* 0.005*,* 0.012 were prepared by solid-state reaction using $SrCO_3$ (99.9+%, Sigma Aldrich Chemie GmbH, Taufkirchen, Germany), TiO_2 (99.9+%, Sigma Aldrich Chemie GmbH, Taufkirchen, Germany) and Fe_2O_3 (99+%, Merck, Darmstadt, Germany) precursors. The A- to B-site molar ratio was kept at 1.0 for all compositions. Zirconia milling balls with a diameter of 2mm and 2-propanol were combined with the precursor mixtures in polyamide jars and subsequently attrition milled for 4 hours at 1000rpm. After milling, the powders were calcined at 975°C for 6 hours in an air furnace to remove CO_2 and form $Sr(Ti_{1-x}Fe_x)O_{3-\delta}$. After calcination, the powders were milled again in a planetary mill with zirconia milling balls of 10mm diameter for 16 hours at 300rpm to break up agglomerates. The final particle sizes of the calcined powders were approximately 500nm.

Bulk polycrystalline pellets of all three compositions were prepared by uniaxial pressing the calcined powders into 13mm cylindrical green bodies under 110MPa pressure. No additives to optimize green body density were used in order to avoid introducing unnecessary impurities. Multiple pellets of each composition were prepared by placement on sacrificial powders of the respective compositions on alumina plates, covered with alumina boats, and sintered in static air or O_2 at 1500°C or 1300°C for 20 hours. It is noted that during cooling from the sintering temperature, the samples were not equilibrated at lower temperatures, and thus the defect state represents something intermediate between that at the sintering temperature and that at a lower temperature where the relevant defect is frozen in. The surfaces of pellets selected for microscopy were prepared by grinding, polishing, and thermal etching at 1200°C for two hours. Additional pellets were ground with an agate mortar and pestle into powders for characterization. The remainder of the text uses shorthand notation of xFe, where x is mol% of Fe in STO.

Room temperature powder X-ray diffraction (XRD)(Malvern Panalytical) was performed on all samples. Lattice pa- rameters were estimated from Rietveld refinement as implemented in the HighScore Plus software (Malvern Panalytical). An XRD standard was not incorporated for calibration, so the lattice parameters are only used for comparison between samples and not for absolute accuracy. Scanning electron microscopy (SEM) (Tescan S8252G) using simultaneous in- beam secondary electron and back scatter electron detectors, as well as, Raman spectroscopy (WiTec, 532nm excitation) were performed at room temperature on polished surfaces of pellets. The Raman spectra were collected from the center of the grains. Room temperature, 298K, X-band electron paramagnetic resonance (EPR) spectroscopy (Bruker ELEXSYS E-500 CW EPR) field swept from 80mT to 450mT was performed on all 1.2Fe samples. An EPR standard was not available for field calibration, so the absolute resonance fields reported are only close estimates and spectra qualitatively used to identify resonant species.

Mössbauer spectra were acquired at 296K with a ^{57}Co–Rh source using a spectrometer operating in the triangular constant-acceleration mode. Each 1.2Fe sample was mounted on an 11mm collimator for all measurements. Due to the small expected resonance signal, samples were made with the maximum amount of powder allowed by the mass absorption of the γ-rays. A Kr-filled proportional counter and a WissEL (Wissenschaftliche Elektronik GmbH,Germany) data acquisition module (CMCA-550 USB) were used to collect and sort the data into 1024 channels. Both the 1.8keV

Kr escape peak and the 14.4keV γ-ray were counted using the two-window pulse-height analysis capability of the module. Samples were run for 3 or 4 days until sufficient counting statistics were obtained (an off-resonance count of about 3×10^6) to allow analysis of the very weak signal. Velocity calibration and the isomer shift zero value were established with a pure

bcc (α)-Fe foil. The counts for each channel (velocity) were normalized (with respect to the total baseline counts) and subspectra were fit to the normalized data using Lorentzian line shapes with WinNormos V3.0 coupled with the IGOR Pro V6.3 software package, also from WissEL.

Magnetometry was performed on all Fe-doped samples using a Magnetic Property Measurement System 3 (MPMS3) (Quantum Design Inc.) operated in DC scan mode. For each sample, approximately 0.5g powder was loaded into a gelatin capsule and mounted inside a clear drinking straw, the typical method for powder measurements. Measurements of mass magnetization as a function of applied magnetic field (M (H)) were performed at 1.8K, 5K, 10K, 20K, and 30K, where the magnitude of magnetization is much greater than the opposing diamagnetic component. To be as accurate as possible, the data was still corrected for contributions from the small diamagnetic background signal arising from the non- magnetic constituents and sample mounting materials. The M (H) curves were fit for the spin magnetic quantum number for a multi-electron species, S, using the relation for magnetization of a paramagnetic species, $M = M_0 B(y)$, where $M_0 = Ng\mu_B S$ is the maximum magnitude of the moment, $B(y)$ is the Brillouin function, and $y = S\mu_0 g\mu_B H/k_B T$.(36) Here, N is the number of magnetic species per kg (allowed to vary during the fit), g is the g-factor (determined by EPR), μ_B is the Bohr magneton value, H is the applied magnetic field, μ_0 is the permeability of vacuum, k_B is Boltzmann's constant, and T is absolute temperature. Measurements of mass susceptibility as a function of temperature were performed from 1.8K to 300K under 0.2T applied magnetic field after cooling in zero field (ZFC), and repeated after cooling under field (FC). Overlaid ZFC/FC curves were used to verify Fe is paramagnetic, *i.e.*, to check for transition temperatures indicating long-range ordering of Fe cations. An additional fitting with the summation of two Brillouin functions was performed on $M(H)$ curves collected at 30K for the 1.2Fe samples to estimate the ratio Fe$^{4+/3+}$ for comparison with EPR and Mössbauer results. For this additional analysis, the individual Brillouin functions were assigned a spin number of 5/2 or 2, for high-spin Fe^{3+} or Fe^{4+}, respectively, and the concentrations of each species allowed to vary during the fit. It should be noted that high-spin Fe^{2+} also has four unpaired electrons and is therefore difficult to distinguish from Fe^{4+}. However, Fe^{4+} has an expected spin-only moment of $4.9\mu_B$ and Fe^{2+} is expected to have a spin-only moment of $5.4\mu_B$.(36)

3 Results

Powder XRD patterns for the four sample sets are shown in Figure 1. All samples were refined to the cubic perovskite structure $Pm\bar{3}m$ and the patterns showed no detectable secondary phases. The refined lattice parameters for all samples are shown in Table 1. The lattice parameters slightly increased above the 0mol% value as Fe-doping increased for all but the 1500°C O_2 sample set.

SEM micrographs of 1.2mol% Fe-doped STO samples sintered in air are shown in Figure 2. Inspection of these representative micrographs reveals that sintering at 1500°C produced slightly larger grain sizes than sintering at 1300°C. Micrographs of all other samples are available in supplementary Figures S1 and S2. Significant microstructural differences related to sintering atmosphere, or Fe-doping at these concentrations, were not observed. Previous work has shown that sintering STO at higher temperatures (1500°C) produces a bi-modal microstructure, which eventually becomes unimodal after enough time.(35) Furthermore, when higher Fe concentrations are present (5mol%), Fe segregation at GBs was shown to induce solute drag effects that result in fine-grained unimodal microstructures.(37)

STO at room temperature is cubic with space group $Pm\bar{3}m$ having 5 atoms per unit cell, each located at a point of inversion symmetry, and no first-order Raman scattering is expected for an ideal crystal.(38) Broken central symmetry due to strain, impurities, and oxygen vacancies, have been shown to cause first-order scattering in cubic STO.(39) Raman spectra of pellets sintered in air at 1300°C are shown in Figure 3, and are representative of all samples, while all other spectra are shown in supplementary Figure S3.

All spectra are largely dominated by broad signals from second-order scattering (two-phonon processes). After a survey of many reported STO Raman spectra, first-order phonon modes have been labeled at their respective locations, whereas second-order modes are marked with stars, in Figure **??**. The single vertical line around 690cm^{-1} was observed to be the only peak that shifted to higher frequency with increased Fe-doping. This peak does not correspond to any possible first order modes and has been previously suggested to indicate the presence of $\mathrm{Fe}_{\mathrm{Ti}}^{\times}$. Doping with Fe appears

to have disrupted the local B-site cubic symmetry enough to allow multiple first-order Raman modes to be observed.

Mössbauer spectra of all four 1.2Fe samples are shown in Figure 4. The asymmetric doublet signals indicate at least two types of Fe sites are present. The solid blue line is the complete spectral fit, while the red line subspectrums were assigned to Fe^{4+} and the green line subspectrums assigned to Fe^{3+}, after comparison with reports in the literature.(40, 41, 42, 43, 44) The site 3 fitted with a single line may be only half of the resonance if it corresponds to a quadrupole doublet with the other half unresolved at a lower velocity resonance. An average of the linewidths from the other two sites was assumed for the site 3 linewidth. There is significant scatter in the data due to large grain sizes, meaning that the samples have less than ideal uniformity. The spectral parameters are listed in Table 2. The linewidths are significantly larger than expected for unique Fe sites, implying there is a distribution of Fe sites centered at each position. This suggests a slight distribution of isomer shifts and quadrupole splittings caused by variations in near neighbor environments.

EPR spectra collected at 298K for all four 1.2Fe samples are shown in Figure 5. The spectra are scaled to have approximately the same intensity at g = 2.0 and a 6× magnification of the low-field regions are inset above each total spectra. Overall, the spectra are dominated by main resonances at the isotropic g = 2.0 field (340mT), with small

satellites on either side owing to 4th-order fine structure interaction.(19) This isotropic signal is due to high-spin Fe^{3+}, as Fe^{4+} and Fe^{2+} are non-Kramers ions and their resonances are not directly observable under the experimental conditions used here, however, their presence does contribute to line broadening.(34) The very weak resonance, at g = 5.9, has been

previously assigned to $\mathrm{Fe}_{\mathrm{Ti}}^{\prime} - \mathrm{V}_{\mathrm{O}}^{\bullet\bullet}\ {}^{\bullet}$ defect associates.(18, 19) The peak intensities in the EPR spectra cannot confirm relative concentrations of each defect state, however, the results confirm that Fe^{3+} species appear to exist as substitutional $\mathrm{Fe}_{\mathrm{Ti}}^{\prime}$ defects not associated with a nearest neighbor $\mathrm{V}_{\mathrm{O}}^{\bullet\bullet}$. Quantitative conclusions about the relative concentrations of EPR silent Fe$^{4+/2+}$ and EPR active Fe^{3+} could not be made due to the lack knowledge of the true concentrations of Fe and the absence of an appropriate spin concentration standard that would otherwise be incorporated into the measurement process.

Measurements of zero-field-cooled (ZFC) and field-cooled (FC) mass magnetic susceptibility *versus* temperature of the 1.2Fe sample sintered at 1500°C in O_2 are superimposed in supplementary Figure S4. This representative example shows the majority of the Fe dopants are paramagnetic centers and long-range magnetic ordering is absent, in other words, no magnetic transition temperatures could be detected, unlike previous results that studied higher Fe concentrations.(15) Examples of possible secondary Fe-containing phases having magnetic ordering could be antiferromagnetic $FeTiO_3$ with T_N = 52K,(45) antiferromagnetic $SrFeO_3$ with T_N = 134K,(46) or one of the many iron oxide phases that are all magnetically ordered. The magnetometry results reported here were not significantly influenced by minority magnetically ordered phases that may have formed under non-equilibrium conditions because all samples displayed only paramagnetic behavior.

Figure 6 shows μ_{eff} /Fe values determined from Brillouin fits of M (H) curves measured at 1.8K, 5K, 10K, 20K and 30K. As temperature decreases to 1.8K, μ_{eff} /Fe decreases for all samples, with the 1.2Fe samples showing the greatest decreases. These observations suggest the presence of negative exchange interactions between paramagnetic species.(47) Decreases in μ_{eff} /Fe at low temperature could also be caused by zero field splitting, however, the EPR spectra for all 1.2Fe samples revealed isotropic *g*-factors for the Fe^{3+} species. Comparison between the different Fe concentrations reveals a general trend of slightly decreasing μ_{eff} /Fe with increasing Fe doping. On each subplot in Figure 6, horizontal dashed and dotted lines mark the expected values for high-spin Fe^{3+} and Fe^{4+}, respectively. The μ_{eff} /Fe values of all 1.2Fe samples correlate well with the EPR determination of the presence of high-spin Fe^{3+}. M (H) curves with Brillouin fits for all samples sintered in air at 1300°C are available in supplementary Figure S5 as a representative example.

Figure 7 shows the estimated $Fe^{4+/3+}$ ratios for all 1.2Fe samples. These values were determined by fitting 30K M (H) curves with two Brillouin functions for the number of magnetic species, N_{3+} and N_{4+}, with S fixed to 2.5 and 2.0 for high- spin Fe^{3+} and Fe^{4+}, respectively. This temperature was chosen for the analysis due to it being far from the decreasing μ_{eff}/Fe values below 10K, where complicated interactions between the Fe cations may affect the results. Sintering in

pure O_2 resulted in more Fe^{4+} than sintering in air. Only the 1.2Fe samples were analyzed by this method for comparison with EPR and Mössbauer results of the same samples. The individual fitted curves are shown in supplementary Figure S6.

4 Discussion

The results presented here demonstrate the challenge in establishing the defect states in dilute Fe-doped STO sintered in an oxidizing environment, and they show that multiple techniques together help provide a comprehensive discription. It is notable that Mössbauer spectra and Raman spectra do not show a difference between samples sintered in O_2 and air, but magnetometry reveals that the ratio of Fe^{4+} to Fe^{3+} is higher in O_2; considering there is not a large difference in P_{O_2} between air and O_2, this result is somewhat unexpected. Previous studies have shown that Fe^{3+} and oxygen vacancies are the main defects in Fe-doped STO in reducing conditions whereas Fe^{4+} is the dominant valence in oxidizing conditions.(29) However, it is noted that because samples prepared in the present study were cooled to room temperature from the sintering temperature, it is difficult to compare the results with other studies that examined conductivity in samples that were equilibrated at lower temperatures (e.g., 700°C - 900°C) since the defect states are expected to change at the lower temperature. (6, 48, 49)

Except for the 1500°C O_2 samples, the lattice parameters of all samples containing Fe all slightly increased with Fe concentration (Table 1). The ionic radii of Fe^{4+} and Fe^{3+} are 0.585Å and 0.645Å, respectively.(50) Comparing these radii with that of Ti^{4+}, 0.605Å, suggests Fe^{3+} is substituted for Ti^{4+}. An alternative explanation for the slight lattice expansion with increasing Fe concentration could be assumed to be caused by additional charge compensating $V_O^{\bullet\bullet}$. However, even for significant oxygen deficit of $\delta = 0.5$, the relative unit cell volume increase would be smaller than 10^{-10}, and therefore oxygen deficiency is likely not the explanation for the lattice parameter change.(51)

It is possible that strontium vacancies (V_{Sr}'') play a role in charge compensation. At the P_{O_2} levels in the present experiments (air and pure O_2), for acceptor-doped STO the concentration of V_{Sr}'' is about 1000 times smaller than the concentration of Fe^{3+} even at temperatures up to 1173K. (7) However, the change of V_{Sr}'' is about half an order of magnitude for a temperature increase of 100 K. Extrapolating this to 1500°C, V_{Sr}'' could reach similar concentrations as Fe^{3+}. However, the defect chemistry of STO is not well-known above 1400°C (52), and it is not clear if such an extrapolation is valid. Accordingly, here, V_{Sr}'' are not expected to affect the lattice parameter; in any case, an increase in V_{Sr}'' would not be expected to lead to a decrease in lattice parameter.

Calculations of defect concentrations by Baker, et al(7) reveal that in dilute Fe-doped STO, the concentration of Fe^{4+} compared to Fe^{3+} (Fe^{4+}/Fe^{3+}) may be significant, consistent with the present observations (Figure 7). Also consistent with the predictions by Baker, et al, the present results reveal that $\mathrm{Fe}^{4+}/\mathrm{Fe}^{3+}$ increases from air to pure O_2, for both temperatures examined here.

Consistent with the description above, Mössbauer spectroscopy results (Figure 4) confirmed that Fe exists in mixed oxidation states for all 1.2Fe samples. The observation of very low-intensity signal with isomer shift of 1.35mm/s in the sample sintered at 1500°C in air could indicate some Fe^{2+} is present, which may exist in a small amount of secondary FeTiO_3 phase, or as a doubly-charged acceptor at the STO B-site. Alternatively, this third species could be another Fe^{3+} sitting in a dramatically different environment than the other Fe^{3+} species. Regardless, the signal of this third site is so low that it is impossible to make a conclusion and it may also exist in the other samples, but was indistinguishable from the background noise. The overall signal intensity for all samples is very low due to only having a natural abundance of the ^{57}Fe isotope. Table 2 shows the estimated fractions of each species (Relative Area), and the majority species in all cases is Fe^{3+}. EPR results confirmed the presence of high-spin Fe^{3+} and revealed the presence of $\mathrm{Fe}'_{\mathrm{Ti}} - \mathrm{V}_{\mathrm{O}}^{\bullet\bullet}$ $^{\bullet}$ defect associates exist in all 1.2Fe samples. The authors note that EPR was not performed on the 0.2Fe and 0.5Fe samples since the main objective of EPR was for the confirmation of the presence of high-spin Fe^{3+} that contributed to the magnetometry results. Previous EPR studies with concentrations of Fe less than 1 percent confirmed that the concentration of Fe-Vo defect complexes increases with decreasing Fe concentrations (18)

The Fe^{4+} species are expected to be randomly substituted for Ti in the STO lattice. Observation of a peak in the Raman spectra near 690cm^{-1} has been previously attributed to Jahn-Teller distortion of the oxygen octahedra around isovalent $\mathrm{Fe}_{\mathrm{Ti}}^{\times}$.(6) In the Raman spectra reported here, this 690cm^{-1} peak sharpens and shifts to higher frequency with increasing Fe concentration. This shift may indicate an average shortening of the Fe−O bonds, consistent with axial elongation of the oxygen octahedra around Fe^{4+}. This observation suggests isovalent $\mathrm{Fe}_{\mathrm{Ti}}^{\times}$ are randomly distributed in the bulk lattice since the Raman spectra were collected from grain interior regions.

Additional evidence for mixed-valence Fe is drawn from the μ_{eff}/Fe values shown in Figure 6. Above 10K, the μ_{eff}/Fe values for all samples are approximately constant with temperature, and the 0.2Fe samples are closest to matching the expected high-spin Fe^{3+} moment (5.9μ_B). As Fe doping increases, μ_{eff} /Fe values slightly decrease. These decreases in μ_{eff}/Fe are proposed to be caused by some fraction of the Fe dopants existing as high-spin Fe^{4+}, which have an expected moment of 4.9μ_B. This assignment correlates with previous computational results by Evarestov *et. al.* that showed the high-spin state for isolated $\mathrm{Fe}_{\mathrm{Ti}}^{\times}$ defects in STO is preferred over the low-spin state.(16) The hypothesis is supported by the Mössbauer results which revealed the presence of Fe^{4+} in all 1.2Fe samples. The $\mathrm{Fe}^{4+/3+}$ ratios shown in Figure 7 provide additional information on the effects of sintering atmosphere. As expected, sintering in pure O_2 produced higher concentrations of Fe^{4+} compared to sintering in air. It should be noted that these results do not rule out the coexistence of Fe^{2+}, as this cation also has 4 unpaired electrons in the high spin state, *i.e.*, $S = 2.0$. Therefore, the relative concentrations of Fe^{4+} shown in Figure 7 may have contributions from Fe^{2+}.

Some final comments are made concerning microstructure development in Fe-doped STO. For high concentrations of Fe, multiple exchange interactions between Fe cations can be present and produce different magnetic behaviors. Zhou proposed that the main interactions are: (1) antiferromagnetic $\mathrm{Fe}^{3+} - \mathrm{O} - \mathrm{Fe}^{3+}$, (2) ferromagnetic $\mathrm{Fe}^{4+} - \mathrm{O} - \mathrm{Fe}^{3+}$, and (3) ferromagnetic $\mathrm{Fe}^{4+} - \mathrm{O} - \mathrm{Fe}^{4+}$.(15) It seems likely that the interactions would vary in the grain boundary regions.

In the presence of positively charged GB cores, $\mathrm{Fe}_{\mathrm{Ti}}^{\prime}$ acceptors accumulate in the space charge region and could exist as next-nearest neighbors.(33, 53) In a recent study, very high Fe concentrations of more than 5 mol% were observed at the GBs by STEM-EDS for dopant concentrations as low as 0.2 mol%. (12) In this study, no evidence for valency changes at the grain boundary were observed by STEM-EELS. However, the sensitivity is comparably low. The grain boundary layer with high Fe concentration was observed to be very thin (~5nm). No second phase formation or amorphous layer was observed at the GBs. More details on the GB structure are not known, but would be of great interest for the understanding of grain boundary motion. It is believed that grain boundary motion in STO is influenced by solute drag, (11, 10, 12, 54) i.e., by the electrostatic interaction of the grain boundary core charge and point defects.

In the present study, some $\mathrm{Fe}_{\mathrm{Ti}}^{\prime}$ acceptors are likely segregated near GBs and exist in configurations of 180° $\mathrm{Fe}^{3+} - \mathrm{O} - \mathrm{Fe}^{3+}$, which leads to interaction (1). In this case, the Fe^{3+} have singly-occupied 3*d* orbitals hybridized with oxygen 2*p* orbitals and interact antiferromagnetically.(36) Negative exchange interactions between $\mathrm{Fe}_{\mathrm{Ti}}^{\prime}$ acceptors could cause the decreasing μ_{eff} /Fe values at low-temperature (Figure 6); the decrease is more pronounced with increasing Fe concentration, supporting the hypothesis that Fe'_{Ti} are interacting at the grain boundaries. While the above description is consistent with a model of acceptor segregation in space charge regions for positively charged grain boundary cores in

STO, more work is needed to establish that interacting Fe^{3+} are concentrated in grain boundary regions. It is recommended to conduct further experiments in which the samples sintered at different temperatures and atmospheres are equilibrated at a lower temperature, i.e. 500-700°C, then quenched to room temperature. Such results could provide a better defined defect equilibrium state and opportunities to compare with other results prepared in a similarly controlled fashion.

5 Conclusions

This work has demonstrated the value in applying EPR, Mössbauer spectroscopy, and magnetometry synergistically to characterize defects states in Fe-doped STO. EPR and Mössbauer provide spectroscopically resolved unique paramagnetic defect states, while magnetometry M(H) and M(T) data provide an integral signal. In other words, the signal detected in the magnetometer is a combined magnetic moment of all magnetic constituents. Therefore, by combining EPR and Mössbauer results with magnetometry results, a more nuanced characterization of the magnetic defect environments can be obtained, when compared to results obtained by each individual technique. This approach is helpful to interpret the slight changes in concentrations of individual magnetic defects (Fe) at such low total doping concentrations. It should be noted that contributions to the signal, in any of the three magnetic characterization techniques employed here, from a small concentration of paramagnetic species in secondary phases (undetected by XRD) can not be resolved. Given the solid solubility of Fe in the $Sr(Ti,Fe)O_3$ system, the contributions from secondary phases are expected to be minimal.

The results here show that dilute Fe dopants in bulk polycrystalline STO exist in mixed-valence states, where some

fraction of Fe^{3+} may be configured as next-nearest neighbors or in a defect complex with an oxygen vacancy. In this dilute limit, it might be assumed that the Fe-dopants can be treated as randomly distributed and non-interacting. However, magnetometry results indicate there exists an interaction between Fe-dopants. Magnetometry was also used to quantify the ratio of Fe^{4+} to Fe^{3+} and to reveal that the amount of Fe^{4+} increases when sintering in O_2 compared with air. This result was unexpected based on the small absolute difference in P_{O_2} between the two sintering atmospheres; however, it highlights the sensitivity of magnetometry and suggests the technique should be included when characterizing low concentrations of paramagnetic defects with EPR or Mössbauer spectroscopy. Acceptor segregation has been previously confirmed by EELS across grain boundaries in STO with excess 0.8 % Ti and 0.2 % Fe at the B-site and with additional Mn diffused into the microstructure. (55, 56) Therefore, in the present work some amount of acceptor dopants are likely segregated at the grain boundaries and may potentially interact with other localized point defects in their vicinity. Estimating valences of Fe-dopants within the 0.2 - 1.2 mol% doping range is difficult. However, magnetometry has been demonstrated as a highly sensitive tool to unify results from EPR and Mössbauer spectroscopy. To the authors best knowledge, this is the first report combining these three techniques to study the valence states of dilute Fe in bulk polycrystalline STO. Future work could examine samples with ^{57}Fe enriched precursor to significantly improve signal of Mössbauer spectra.

6 Acknowledgments

The authors acknowledge Dr. Serena Eley (CSM) for access to the MPMS3, Dr. Don Williamson (CSM) for collecting the Mössbauer spectra, and Dr. Ron Goldfarb (NIST) for providing magnetometry advice. MK acknowledges support by the National Science Foundation Graduate Research Fellowship Program (NSFGRFP). MK and IR acknowledge support by the National Science Foundation award DMR-1563754. WR and JP acknowledge support by the German Research Foundation under grants no. HO 1165/20 and RH 146/1. The Tescan S8252G instrument used in this research was purchased through National Science Foundation MRI award DMR-1828454.

References

[1] Szot K, Speier W, Bihlmayer G, Waser R. Switching the electrical resistance of individual dislocations in sigle- crystalline $SrTiO_3$. Nat Mat 2006;5:312-320.

[2] Gryaznov D, Fleig J, Maier J. Numerical study of grain boundary diffusion in nanocrystalline ionic materials including blocking space charges. Solid State Ion 2006;177:1583-1586.

[3] Ohta H, Kim S, Mune Y, Mizoguchi T, Nomura K, Ohta S *et al.* Giant thermoelectric Seebeck coefficient of a two-dimensional electron gas in $SrTiO_3$. Nat Mat 2007;6:129-134.

[4] Reyren N, Thiel S, Caviglia AD, Fitting Kourkoutis L, Hammerl G, Richter C *et al.* Superconducting Interfaces Between Insulating Oxides. Science 2007;317:1196-1200.

[5] Phoon BL, Lai CW, Juan JC, Show PL, Pan GT. Recent developments of strontium titanate for photocatalytic water splitting application. Int J Hydrogen Energy 2019;44:14316-14340.

[6] Vracar M, Kuzmin A, Merkle R, Purans J, Kotomin EA, Maier J *et al.* Jahn-Teller distortion around Fe^{4+} in $SrFe_xTi_{1-x}O_{3-\delta}$ from x-ray absorption spectroscopy, x-ray diffraction, and vibrational spectroscopy. Phys Rev B 2007;76:174107.

[7] Baker JN, Bowes PC, Long DM, Moballegh A, Harris JS, Dickey EC *et al.* Defect mechanisms of coloration in Fe-doped $SrTiO_3$ from first principles. Appl Phys Lett 2017;110:122903.

[8] Tang AS, Pelliciari J, Song Q, Song Q, Ning S, Freeland JW *et al.* XMCD study of magnetism and valence state in iron-substituted strontium titanate. Phys Rev Mat 2019;3:054408.

[9] Lemke F, Rheinheimer W, Hoffmann MJ. Sintering and grain growth in $SrTiO_3$: impact of defects on kinetics. Journal of Ceramic Society of Japan 2016;124:346-353.

[10] Rheinheimer W, Hoffmann MJ. Grain growth in perovskites: What is the impact of boundary transitions? Current Opinion in Solid State and Materials Science 2016;20:286-298 .

[11] Rheinheimer W, Parras JP, Preusker J-H, De Souza RA, Hoffmann MJ. Grain growth in strontium titanate in electric fields: the impact of space charge on the grain boundary mobility. J Amer Ceram Soc 2019;102:3779– 3790.

[12] Zahler MP, Kraschewski SM, Störmer H, Gerthsen D, Bäurer M, Rheinheimer W. Grain growth and segregation in Fe-doped SrTiO3: Experimental evidence for solute drag. J Europ Ceram Soc 2023;43:1613-1624.

[13] De Souza RA. The formation of equilibrium space-charge zones at grain boundaries in the perovskite oxide $SrTiO_3$. Phys Chem Chem Phys 2009;11:9939-9969.

[14] Rothschild A, Menesklou W, Tuller HL, Ivers-Tiffee E. Electronic structure, defect chemistry, and transport prop- erties of $SrTi_{1-x}Fe_xO_{3-y}$ solid solutions. Chem Mat 2006;18:3651-3659.

[15] Zhou H, Goodenough J. Polaron morphologies in $SrFe_{1-x}Ti_xO_{3-\delta}$. J Solid State Chem 2004;177:1952-1957.

[16] Evarestov RA, Piskunov S, Kotomin EA, Borstel G. Single impurities in insulators: Ab initio study of Fe-doped $SrTiO_3$. Phys Rev B 2003;67,064101.

[17] Merkle R, Maier J. How is oxygen incorporated into oxides? A comprehensive kinetic study of a simple solid-state reaction with $SrTiO_3$ as a model material. Angew Chem Int Ed 2008;47:3874-3894.

[18] Merkle R, Maier J. Defect association in acceptor-doped $SrTiO_3$: case study for $Fe'_{Ti}V_{O}^{\bullet\bullet}$ and $Mn''_{Ti}V_{O}^{\bullet\bullet}$. Phys Chem Chem Phys 2003;5:2297-2303.

[19] Drahus MD, Jakes P, Erdem E, Eichel RA. Defect structure of the mixed ionic-electronic conducting $Sr(TiFe)O_x$ solid-solution system - Change in iron oxidation states and defect complexation. Solid State Ion 2011;184:47-51.

[20] Faughnan BW. Photochromism in Transition-Metal-Doped SrTiO$_3$. Phys. Rev. B. Condens. Matter 1971;4:3623- 3636.

[21] Schirmer OF, Berlinger W, Miller KA. Electron Spin Resonance and Optical Identification of $Fe^{4+} - V_O$ in SrTiO. Solid Slate Commun 1975; 16: 1289-12392.

[22] Waser R, Bieger T, Maier J. Determination of acceptor concentrations and energy levels in oxides using an optoelec- trochemical technique. Solid Slate Commun 1990; 76: 1077-1081.

[23] Waser R, Baiatu T, Härdtl K-H. dc electrical degradation of perovskite-type titanates: III, a model of the mechanism.

J Amer Ceram Soc 1990;73:1663-1673

[24] Suziki I, Gura L, Klein A. The energy level of the $Fe^{2+/3+}$-transition in BaTiO$_3$ and SrTiO$_3$ single crystals. Phys.

Chem. Chem. Phys 2019; 21: 6238-6246

[25] Blanc J, Staebler Dl. Electrocoloration in SrTiO$_3$ - vacancy drift and oxidation-reduction of transition metals. Phys Rev B 1971; 4:3549

[26] Hong K, Lee TH, Suh JM, Yoon, S-H, Jang HW. Perspectives and challenges in multilayer ceramic capacitors for next generation electronics. J Mat Chem C 2019; 9782-9802

[27] Waser R, Dittmann R, Staikov G, Szot K. Redox-based resistive switching memories - nanoionic mechanisms, prospects, and challenges perspectives and challenges in multilayer ceramic capacitors for next generation electronics.

Advanced Materials 2009;21: 2632-2663

[28] Yoo HI, Chang M-W, Oh T-S, Lee C-E, Becker KD. Electrocoloration and oxygen vacancy mobility of BaTiO$_3$. J Appl Phys 2007;102

[29] Lenser K, Kalinko A, Kuzmin A, Berzins D, Purans J, Szot, KI, Waser R, Dittman R. Spectroscopic study of the electric field induced valence change of Fe-defect centers in $SrTiO_3$. Phys. Chem. Chem. Phys 2011;13:20779-20786

[30] Müller KA. Critical phenomena near structural phase transitions studied by EPR. Ferroelectrics 1974;7:17-21.

[31] Knauer U. Distribution of the iron dopant in barium titanate ceramic, determined by the scanning transmission electron microscope. Phys Stat Sol (a) 1979;53:207-210.

[32] Desu SB, Payne DA. Interfacial eegregation in perovskites: II, experimental evidence. J Am Ceram Soc 1990;73(11):3398-3406.

[33] Chiang YM, Takagi T. Grain-boundary chemistry of barium titanate and strontium titanate: I, high-temperature equilibrium space charge. J Am Ceram Soc 1990;73(11):3278-3285.

[34] Abragam A, Bleaney B. Electron paramagnetic resonance of transition ions. 1st ed. Oxford: Clarendon Press; 1970.

[35] Rheinheimer W, Hoffman MJ. Non-Arrhenius behavior of grain growth in strontium titanate: New evidence for a structural transition of grain boundaries. Scripta Materialia 2015;101:68-71.

[36] Coey JMD. Magnetism and Magnetic Materials. 1st ed. Cambridge: Cambridge University Press; 2009.

[37] Vikrant KSN, Rheinheimer W, Sternlicht H, Bäurer M, Garćia RE. Electrochemically-driven abnormal grain growth in ionic ceramics. Acta Materialia 2020;200:727-734.

[38] Nilsen WG, Skinner JG. Raman spectra of strontium titanate. J Chem Phys 1968;48(5):2240-2248.

[39] Balachandran U, Eror NG. Raman spectra of strontium titanate. Comm Am Cer Soc 1982;April:54-46.

[40] Bhide VG, Bhasin HC. Mössbauer studies of the $SrTiO_3$:Fe^{57} system. Phys Rev 1968;172:290-294.

[41] Luiskutty CT, Ouseph PJ. Valence states of iron in photochromic strontium titanate by Mössbauer effect. Solid States Comms 1973;13:405-409.

[42] Multani M. Ultra-stable high-precision Mössbauer spectroscopy of photochromic centers in Fe:$SrTiO_3$. Mat Res Bull 1984;19:25-34.

[43] Dulov EN, Ivoilov NG, Strebkov OA, Tagirov LR, Nuzhdin VI, Khaibullin RI *et al.* Magnetic phase composition of strontium titanate implanted with iron ions. Mat Res Bull 2011;46:2304-2307.

[44] Goto T, Kim DH, Sun X, Onbasli MC, Florez JM, Ong SP *et al.* Magnetism and faraday rotation in oxygen-deficient polycrystalline and single-crystal iron-substituted strontium titanate. Phys Rev Appl 2017;7:024006.

[45] Raghavender AT, Hong NH, Lee KJ, Jung MH, Skoko Z, Vasilevskiy M *et al.* Nano-ilmenite $FeTiO_3$: synthesis and characterization. J Magn Magn Mater 2013;331:129-132.

[46] Takeda T, Yamaguchi Y, Watanabe H. Magnetic Structure of $SrFeO_3$. J Phys Soc Jpn 1972;33:967-969.

[47] Boca R, Titis J. Magnetostructural D-correlation for zero-field splitting in nickel(II) complexes. In: Cartere TW, Verley KS, editors. Coordination Chemistry Research Progress. New York, USA: Nova Science Publishers; 2008. p. 247-304.

[48] Waser Bulk conductivity and defect chemistry of acceptor-doped strontium titanate in the quenched state. J Am Ceram Soc 1991;74:1934-1940.

[49] Maier R A, Randall C A Low-temperature ionic conductivity of an acceptor-doped perovskite: 1. impedance of single-crystal $SrTiO_3$. J Am Ceram Soc 2016; 99:3350-3359.

[50] Shannon RD. Revised Effective Ionic Radii and Systematic Studies of Interatomic Distances in Halides and Chalco- genides. Acta Cryst 1976;A32:751-767.

[51] Freedman DA, Roundy D, Arias TA. Elastic effects of vacancies in strontium titanate: Short- and long-range strain fields, elastic dipole tensors, and chemical strain. Phys. Rev. B 2009, 80, 064108.

[52] Moos R, Hardtl KH. Defect chemistry of donor-doped and undoped strontium titanate ceramics between 1000 °and 1400 °C. J Amer Ceram Soc;80:2549-2562.

[53] Klie RF, Browning ND. Atomic scale characterization of oxygen vacancy segregation at $SrTiO_3$ grain boundaries. Appl Phys Lett 2000;77:3737–3739.

[54] Benrabah I-E, Van Landeghem HP, Bonnet F, Denand B, Geandier G, Deschamps A. ”Solute drag modeling for ferrite growth kinetics during precipitation experiments”, Acta Materialia 2021; 221: 117364

[55] Wilcox, N, Ravikumar, V, Rodrigues, RP, Dravid, VP, Vollmann, M, Waser, R, Soni, KK, Adriaens, AG. Investi- gation of grain boundary segregation in acceptor and donor doped strontium titanate. Solid State Ionics 1995; 75: 127-136.

[56] V Ravikumar, V, Rodrigues, RP, Dravid, VP. An investigation of acceptor-doped grain boundaries in acceptor and donor doped strontium titanate. Journal of Physics D: Applied Physics 1996; 29: 1799.

List of Figures

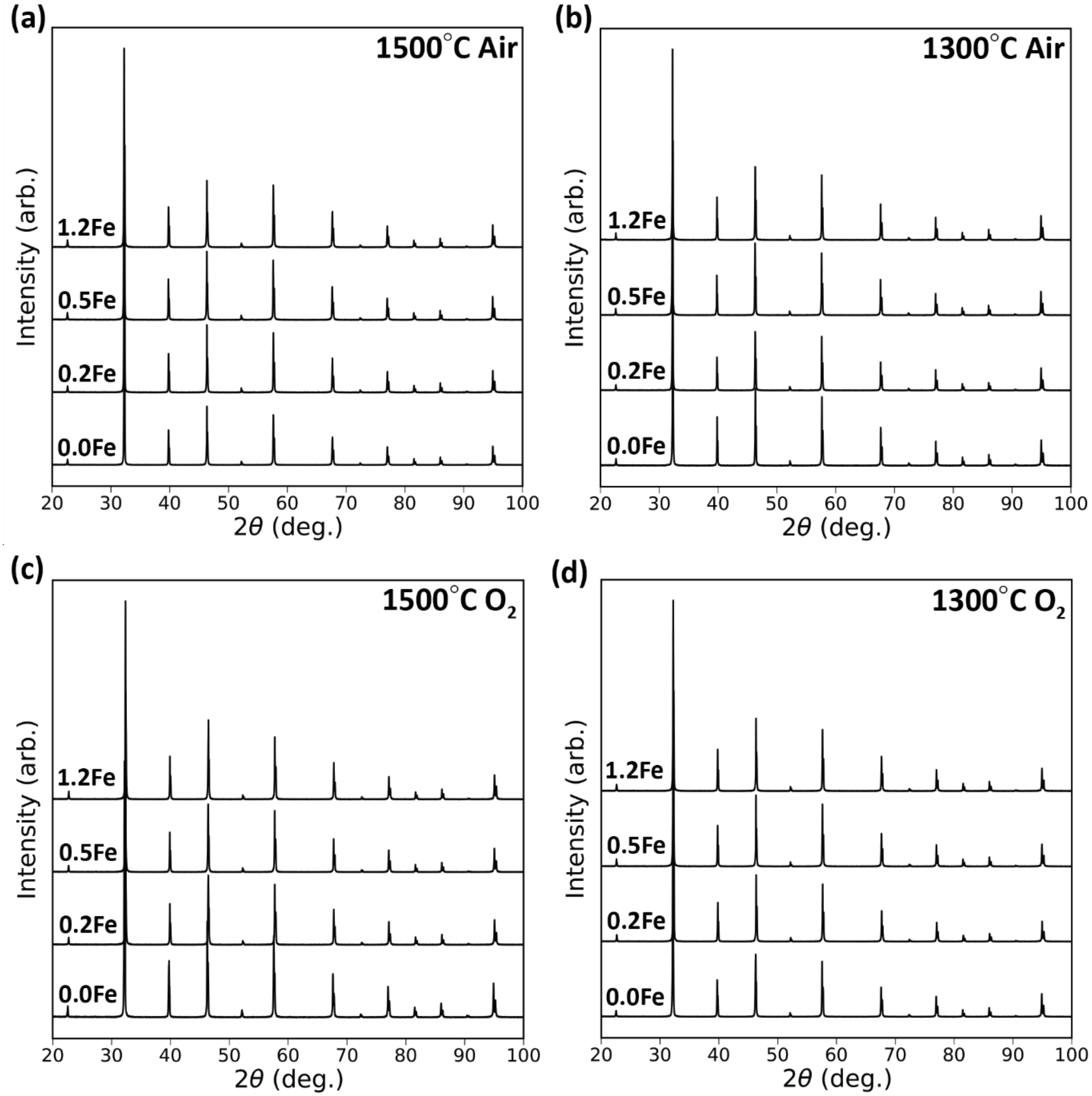

Figure 1. Room temperature powder X-ray diffraction patterns of the four sample sets: (a) air sintered at 1500°C,

(b) air sintered at 1300°C, (c) O_2 sintered at 1500°C, and (d) O_2 sintered at 1300°C. All samples were refined to the cubic perovskite_structure $Pm3m$ and no detectable secondary phases were observed.

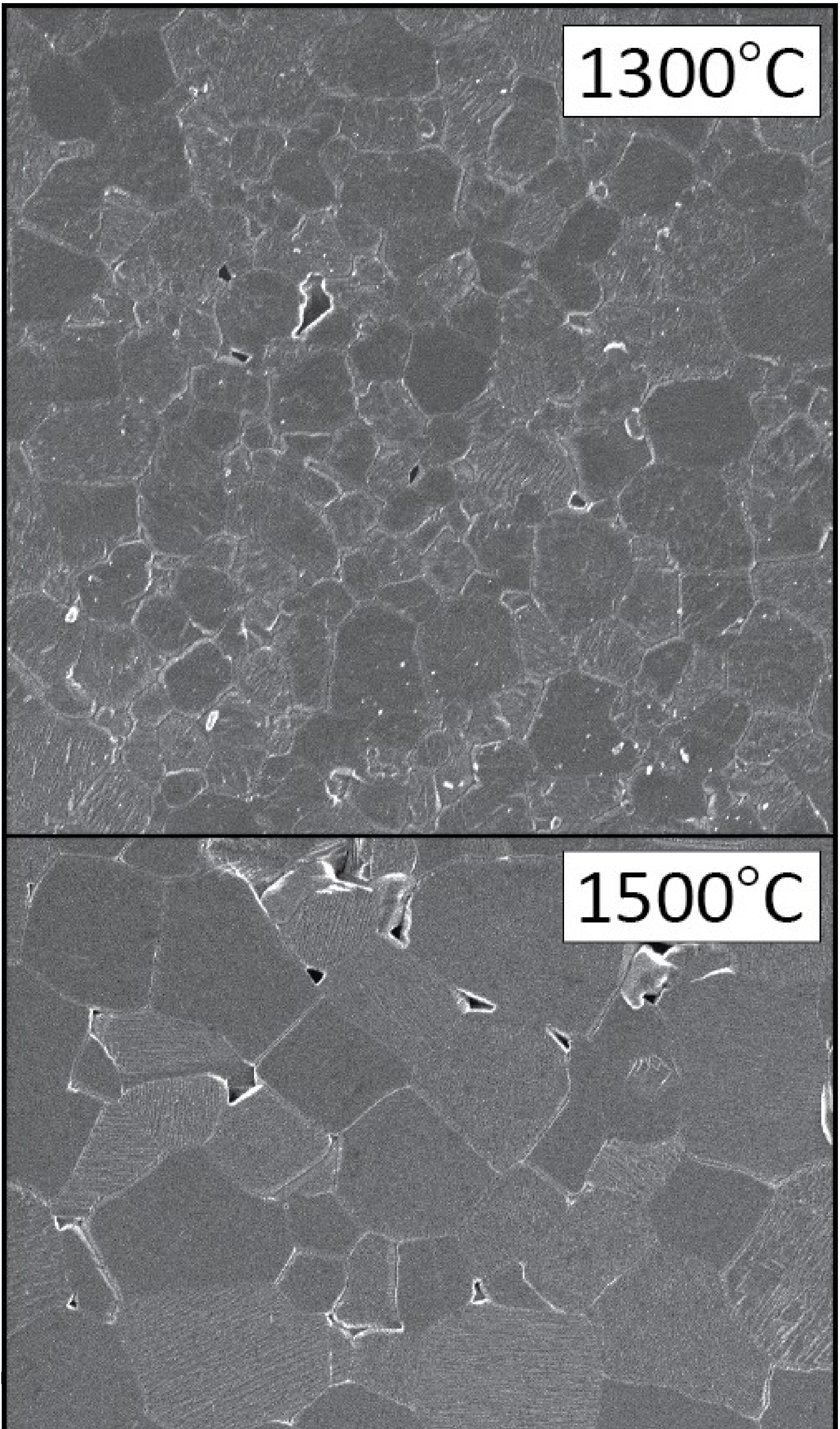

Th

Figure 2. SEM micrographs of 1.2mol% Fe-doped STO samples sintered in air. This representative example shows how sintering at 1500°C produced slightly larger grains than sintering at 1300°C . Micrographs of all other samples are available in the supplementary information.

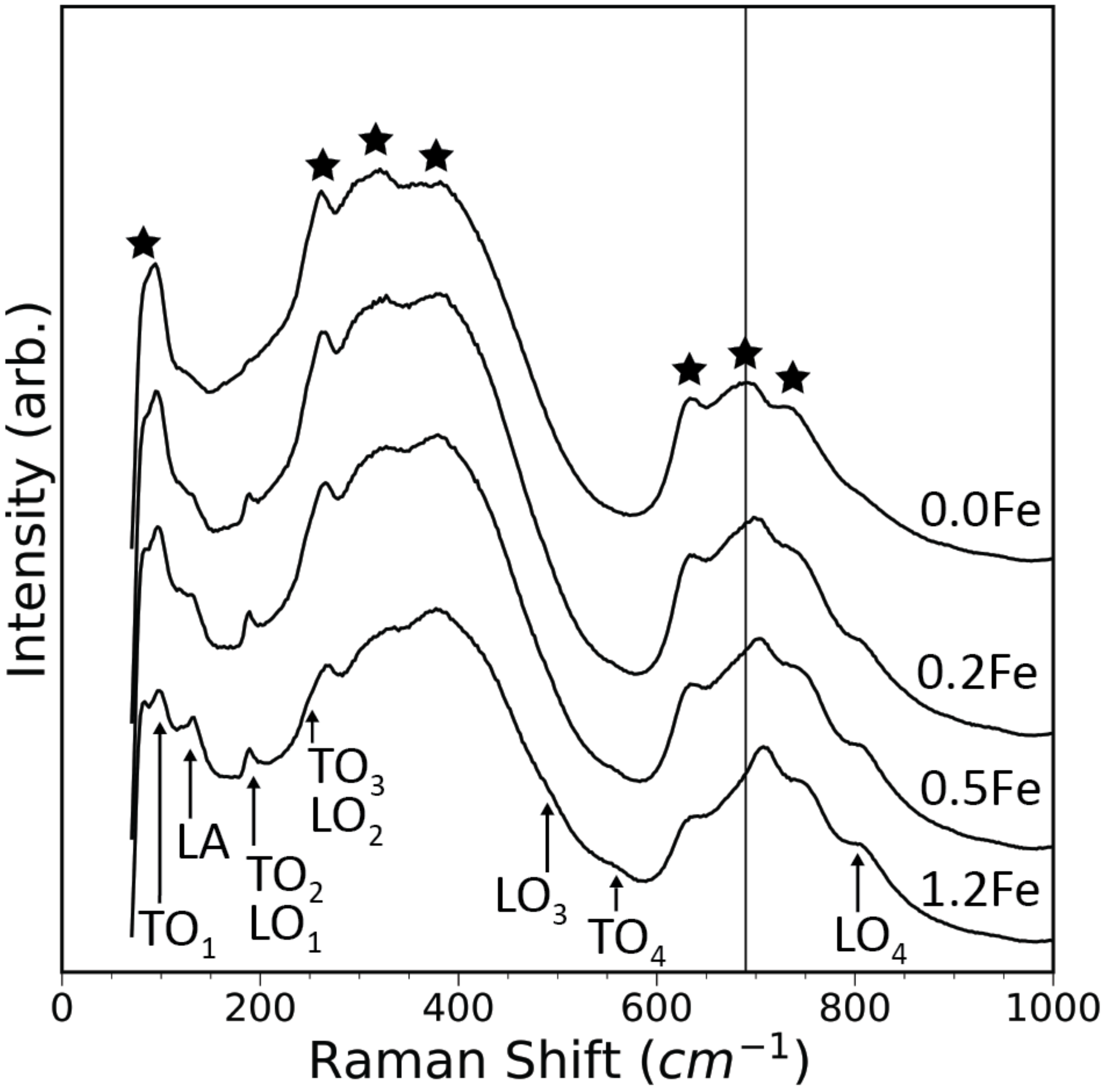

Figure 3. Raman spectra of pellets sintered in air at 1300°C as a representative example. Spectra were collected from grain interior regions of polished surfaces. The spectra are dominated by broad second-order modes (stars), however, the appearance of first order modes (labelled) is connected to slight disruption of ideal cubic symmetry by incorporation of Fe. The single vertical line at 690cm^{-1} indicates the location of a peak previously connected to substitutional Fe^{4+}.(6)

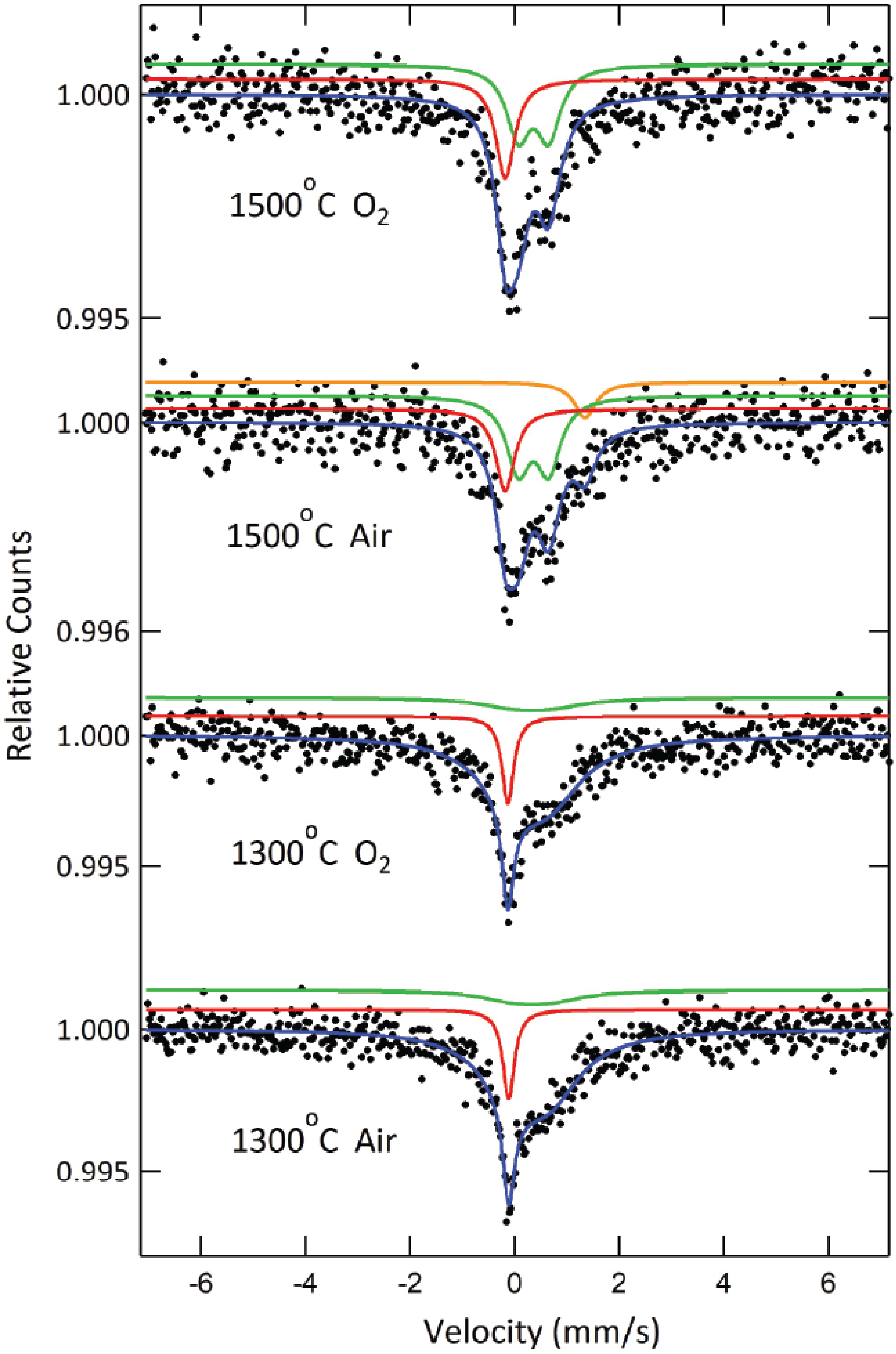
1.000
0.995
1.000
0.996
1.000
0.995
1.000
0.995
1500°C O$_2$
1500°C Air
1300°C O$_2$
1300°C Air
Relative Counts
-6
-4
-2
0
2
4
6
Velocity (mm/s)

Figure 4. Mössbauer spectra of all four 1.2mol% Fe-doped STO samples. The blue line is the least squares fit of the total spectra, while the green and red subspectrums were assigned to Fe^{3+} and Fe^{4+}, respectively. The third subspectrum (yellow) in the 1500°C air-sintered sample may indicate a small concentration of Fe^{2+}, or Fe^{3+} in a dramatically different local environment, but this assignment is inconclusive.

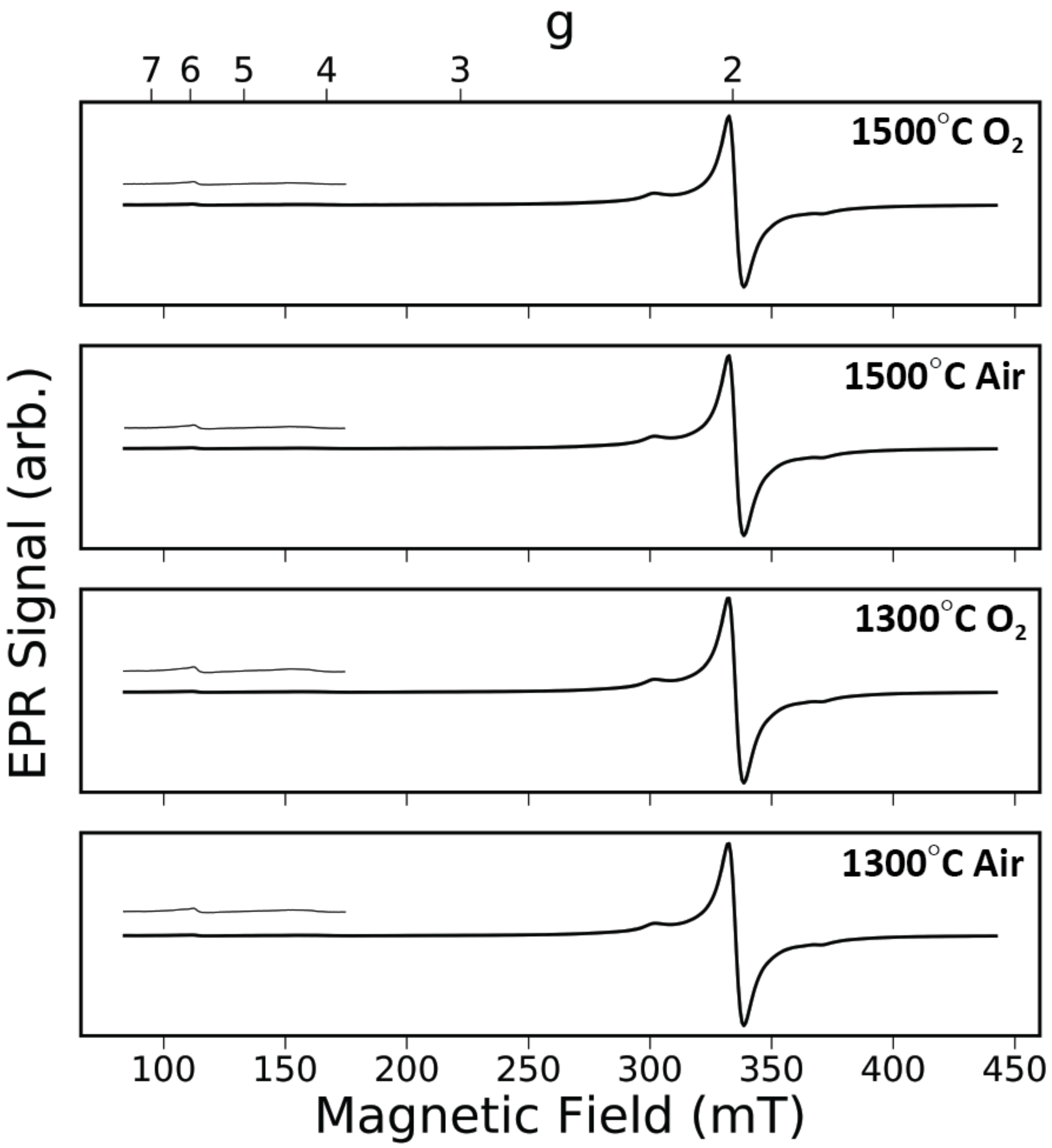

Figure 5. Room temperature X-band electron paramagnetic resonance spectra of all four 1.2mol% Fe-doped STO samples. Nearly all the Fe^{3+} resonate at the isotropic *g* = 2 field (340mT), however, a low-intensity resonance around *g* = 5.9 was also observed. This region is magnified by 6× and inset above each total spectra. This has been previously shown to be a signature of $\mathrm{Fe}_{\mathrm{Ti}}' - \mathrm{V}_{\mathrm{O}}^{\bullet\bullet}\ ^{\bullet}$ defect associates.(18, 19, 30)

Figure 6. μ_{eff} /Fe values estimated from Brillouin fits of *M* (*H*) curves measured at 1.8K, 5K, 10K, 20K and 30K. Decreases at low-temperature may indicate the presence of negative exchange interactions. Horizontal dashed and dotted lines mark the expected spin-only moments for high-spin Fe^{3+} and Fe^{4+}, respectively.

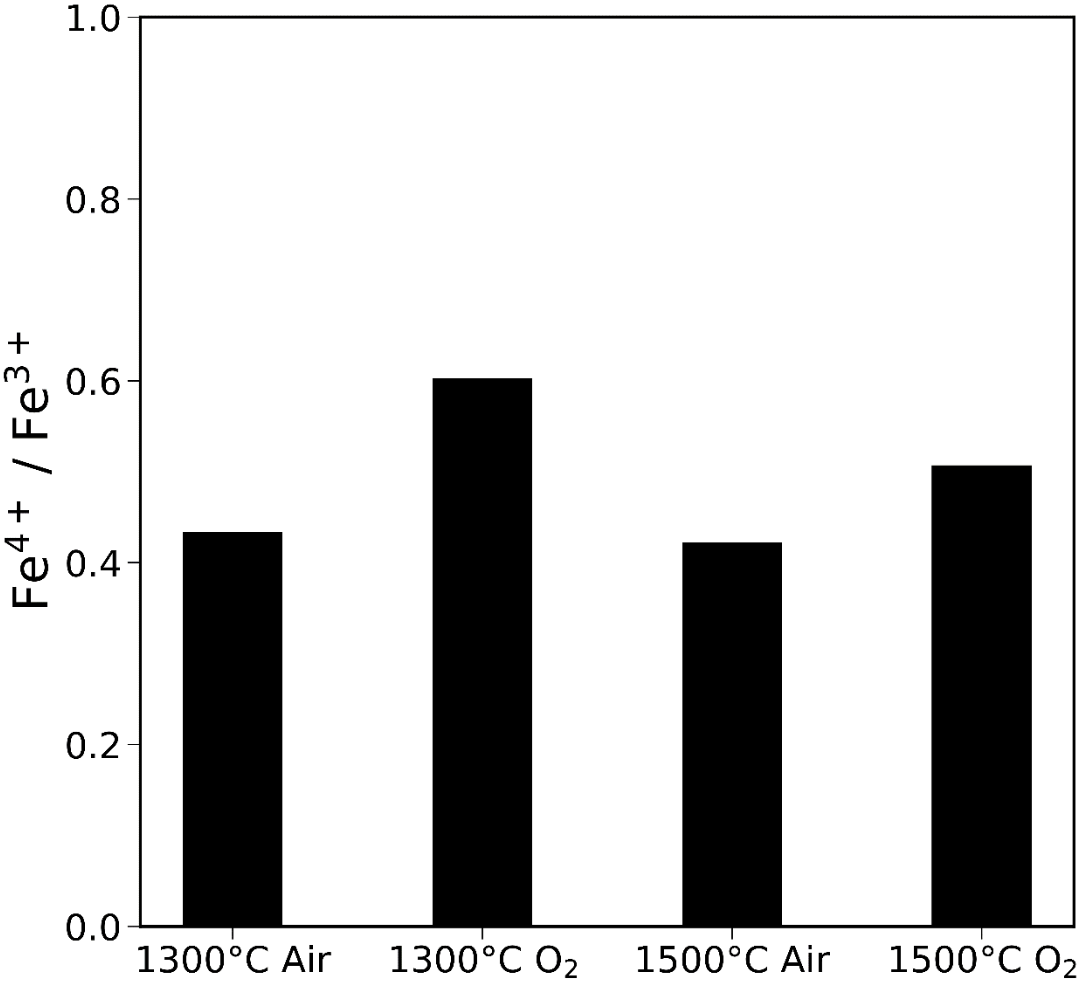

Figure 7. Estimated ratio of Fe^{4+} to Fe^{3+} in each of the 1.2mol% Fe-doped STO samples. Values were determined by fitting 30K *M* (*H*) curves with two Brillouin functions for the number of magnetic species, $N_{5/2}$ Fe^{3+} and N_2 Fe^{4+} , with *S* values of the high-spin state fixed at 5/2 and 2, respectively. It should be noted that, Fe^{2+} also has *S* = 2 and, if present, would contribute to the Fe^{4+} content by this method.

Tables

Cubic Lattice Parameters of all Samples

	a_{0Fe}(Å)	$a_{0.2Fe}$(Å)	$a_{0.5Fe}$(Å)	$a_{1.2Fe}$(Å)
1300°C Air	3.90799(1)	3.90822(1)	3.90860(1)	3.90874(1)
1500°C Air	3.90812(1)	3.90818(1)	3.90863(1)	3.90872(1)
1300°C O_2	3.90787(1)	3.90820(1)	3.90860(1)	3.90867(1)
1500°C O_2	3.90799(1)	3.90631(2)	3.90698(1)	3.90684(1)

Table 1: Cubic lattice parameter (a) of Fe-doped STO samples sintered in air or O_2 at 1500°C or 1300°C. The values were determined by Rietveld refinement of powder X-ray diffraction data shown in Figure 1. The uncertainties of the last digits are displayed in parenthesis.

Mössbauer Spectroscopy Results

Sample	Fe Site	Isomer Shift (mm/s)	Quadrupole Splitting (mm/s)	Linewidth (mm/s)	Relative Area (%)
1500°C O_2	Fe^{4+} (red)	-0.18(2)	0	0.44(4)	32(6)
	Fe^{3+} (green)	0.36(3)	0.58(6)	0.55(3)	68(6)
1500°C Air	Fe^{4+} (red)	-0.18(f)	0	0.44(f)	24(7)
	Fe^{3+} (green)	0.36(f)	0.58(f)	0.55(f)	63(7)
	Site 3 (yellow)	1.35(10)	0	0.5(f)	13(7)
1300°C O_2	Fe^{4+} (red)	-0.13(1)	0	0.27(5)	15(3)
	Fe^{3+} (green)	0.33(4)	0.7(2)	1.6(2)	85(7)
1300°C Air	Fe^{4+} (red)	-0.12(1)	0	0.27(4)	15(3)
	Fe^{3+} (green)	0.34(3)	0.7(2)	1.5(2)	85(6)

Table 2: Fitted parameters from all four 1.2Fe Mössbauer spectra. Uncertainty in the last significant figure is in paren- theses, where some values were fixed (f) in the sample having 3 Fe sites. Isomer shift is given

relative to the center of the pure Fe calibration spectrum and minimum linewidth obtainable from the spectrometer is 0.23 mm/s.